Article

The Momentum Transfer Mechanism of a Landslide Intruding a Body of Water

Zhenzhu Meng [1,2], Jianyong Hu [3,*], Jinxin Zhang [1,2], Lijuan Zhang [4] and Zhenxia Yuan [5]

1   School of Water Conservancy and Environment Engineering, Zhejiang University of Water Resources and Electric Power, Hangzhou 310018, China; mengzhzh@zjweu.edu.cn (Z.M.); zhangjx@zjweu.edu.cn (J.Z.)
2   Key Laboratory for Technology in Rural Water Management of Zhejiang Province, Hangzhou 310018, China
3   School of Geomatics and Municipal Engineering, Zhejiang University of Water Resources and Electric Power, Hangzhou 310018, China
4   Huai'an Water Conservancy Survey and Design Institute Co., Ltd., Huai'an 223005, China; zhanglijuan-ha@bewg.net.cn
5   School of Civil Engineering and Architecture, Zhongyuan University of Technology, Zhengzhou 450007, China; 6570@zut.edu.cn
*   Correspondence: hujy@zjweu.edu.cn

Abstract: Landslide-generated waves occur as a result of the intrusion of landslides such as mud flows and debris flows into bodies of water such as lakes and reservoirs. The objective of this study was to determine how the momentum is transferred from the sliding mass to the body of water on the basis of theoretical analysis and physical model experiments. Considering the viscoplastic idealization of natural landslides, the theoretical model was established based on the momentum and mass conservation of a two-phase flow in a control volume. To close the theoretical equations, slide thickness and velocity passing through the left boundary of the control volume were estimated by lubrication theory, and the interaction forces between the slide phase and water phase, including hydrostatic force and drag force, were given by semiempirical equations fitted with experimental data obtained using the particle image velocimetry (PIV) technique. The near-field velocity fields of both the sliding mass and the body of water, as well as the air–water–slide interfaces, were determined from the experiments. The theoretical model was validated by comparing the theoretical and experimental data of the slide thickness and slide velocity, as well as the momentum variations of the two phases in the control volume.

Keywords: momentum transfer; landslide-generated waves; PIV; viscoplastic material; interaction force; Carbopol

1. Introduction

Landslides such as avalanches, debris flows, mud flows, glacier calving, and rockfalls are common in mountainous regions. When these masses intrude the surrounded bodies of water such as mountain lakes, reservoirs, rivers, and oceans, they can generate large impulse waves (also called landslide-generated waves or landslide tsunamis) that can have devastating effects. The problem of landslide-generated waves has attracted considerable attention in recent decades. Many of the physical insights into this phenomena have come from laboratory scale-down experiments [1–3] and to a lesser extent from theoretical models [4,5], numerical simulations [6–8], and field data surveys [9–11].

Laboratory experiments not only make it possible to shed light on the physical processes that govern the wave generation, but they also allow us to quantify how waves' features such as amplitude and height depend on the initial conditions of the incoming sliding mass. In most earlier studies, these quantitative analyses combined dimensional analysis and nonlinear regression techniques [12–15]. The studies have occasionally involved a scale analysis of the governing equations [16–18]. For both of the two above-mentioned approaches, the modeling of the wave characteristics has mostly relied on empirical equations

in the form of power functions of several selected dimensionless parameters that pertained to the momentum flux of the incoming sliding mass.

However, the physical mechanism governing the slide–water interaction lacks understanding. Zitti et al. (2016) studied how mass and momentum were exchanged between the incoming sliding material flow and the outgoing impulse wave by using a control volume surrounding the impact zone [5]. By scaling the mass and momentum balance equations, they obtained dimensionless numbers that could subsequently be used for correlating wave features with initial parameters. Miller et al. (2017) and Franz et al. (2021) discussed the effects of momentum transfer on wave features and landslide deposit by experiments and numerical simulations, respectively [19,20]. Mulligan (2017) provided a simplified theoretical expression based on the momentum flux of the sliding mass on impact [3]. Kim et al. (2020) established a theoretical expression for the hydrostatic pressure and Coulomb-type friction force in their numerical work [21].

Even though a series attempts have been performed to understand the physics behind the impacting process, the experimental support for discovering the internal dynamics of the slide–water interaction is lacking. The laboratory challenge is to measure the internal velocities of the sliding mass and the water body during the impacting process. Using the PIV technique, previous studies have measured the near-field velocity field of the body of water during the intrusion of a landslide [22]. However, the velocity field of the submerged slide material has been lacking until now, due to the difficulty of finding a slide material that is transparent and that can easily be traced in PIV measurements. Previous studies commonly approximated the velocity of the sliding mass by its frontal velocity passing through the shoreline. It was logical to assume that the block slide passed through the shoreline at a constant velocity. Yet, for other sliding masses, which behave similarly to a long and thin train of material, the velocity at the shoreline was found to vary with time [23].

The choice of material used for the landslide is a problem that needs to be considered in all experimental studies. Blocks and granular materials have been routinely used for mimicking landslides at the laboratory scale [24–26]. To investigate the rheology of gravity-driven flows such as mud flows, debris flows, and avalanches, in addition to granular flows, scientists have developed an analogy with yield stress fluids, whose rheological behaviors can be described by viscoplastic models such as the Bingham model and Herschel–Bulkley model [27–29]. Following the viscoplastic idealizations of natural landslides, we introduced a viscoplastic material called Carbopol, which is one of the best-suited materials for the Herschel–Bulkley model, into experiments of landslide-generated waves [30–32]. One advantage of Carbopol is that it is transparent and can be easily seeded with tracing particles without changing the rheological properties so that its internal velocity can be measured using the PIV technique.

The objective of this study was to determine the momentum transfer mechanism governing a landslide intruding a body of water. A theoretical model for viscoplastic fluid interacting with the body of water was developed. We first revisited the governing equations developed by Zitti et al. (2016) [5], which were based on the mass and momentum conservations of a two-phase flow in a control volume. The slide thickness and velocity at the left boundary of the control volume were given by the lubrication model and kinematic wave model, respectively [33]. Then, using Carbopol as the slide material, we provided a novel experimental method based on the PIV technique to measure the near-field velocity fields of the sliding mass and the body of water simultaneously. The interaction forces between the two phases, including drag force and hydrostatic force, were given by semiempirical equations fitted using experimental data. Then, the momentum variations of the two phases were analyzed.

2. Theoretical Model

2.1. Physical Model

Figure 1 illustrates the two-dimensional physical model of a landslide moving down a slope and intruding a body of water. The whole process can be divided into three stages: in the first stage, the slide is at rest in the container box, and then it starts moving; in the second stage, it moves down the slope and reaches the shoreline; in the third stage, it enters the body of water and generates waves. We considered a slope with an inclination of θ entering into a horizontal flume filled with water. The still water depth is denoted by h_0, the free water surface is denoted by η, and the water density is denoted by ρ_w. A slide mass, with a volume of V_I and a density of ρ_s, is released at a distance of l_s from the shoreline. The slide's initial shape is idealized as a trapezoid with a height of s_0 and length of l_0, with the top surface parallel to the free water surface. The volume of the immersed slide is denote by V_s. The wave created by the incursion of the sliding mass is mainly evaluated by its height h and amplitude a.
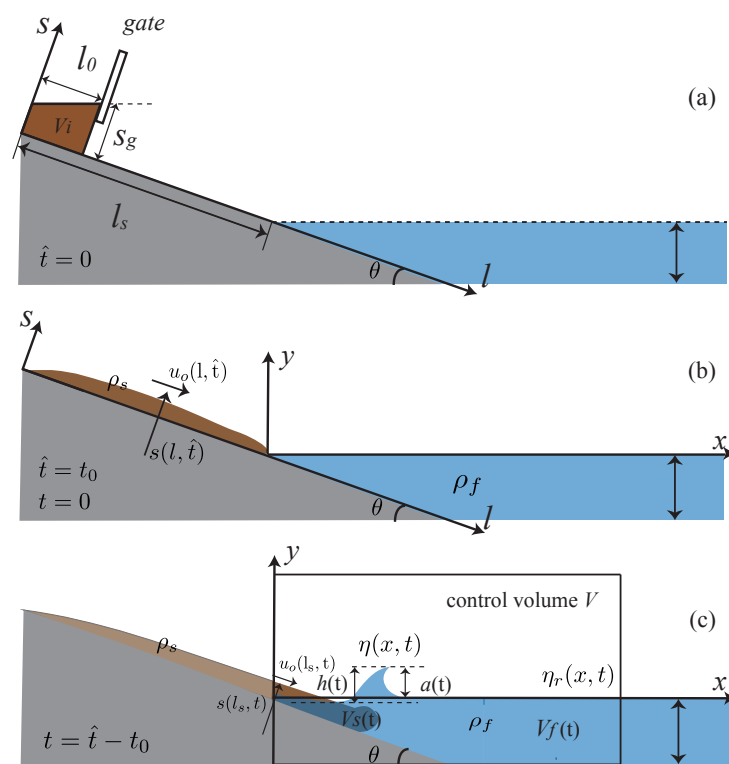
Figure 1. Sketch of the physical model: (**a**) still landslide, (**b**) moving sliding mass on the slope, (**c**) landslide entering water.

2.2. Momentum Conservation of Two Phase Flow in a Control Volume

Following Zitti et al. (2016) [5], we first considered the mass and momentum balance equations in a control volume V. As shown in Figure 1c, the control volume V consists of three phases: the slide phase, water phase, and air phase. Mass and momentum balance equations with the fixed volume V for each phase can be written in an integral form:

$$\frac{d}{dt} \int_{V_m} \alpha_i \rho_i dV_m = \frac{d}{dt} \int_V \alpha_i \rho_i dV + \int_S \alpha_i \rho_i (\mathbf{u}_i \cdot \mathbf{n}) dS = 0 \tag{1}$$

$$\frac{d}{dt} \int_{V_m} \alpha_i \rho_i \mathbf{u}_i dV_m = \frac{d}{dt} \int_V \alpha_i \rho_i \mathbf{u}_i dV + \int_S \alpha_i \rho_i u_i (\mathbf{u}_i \cdot \mathbf{n}) dS = \mathbf{F} \tag{2}$$

where the subscript i = s, f refers to the slide or fluid phase, V_m is the material volume, α_i is the fraction of the volume occupied by phase i, ρ_i denotes the density of each phase,

and $\mathbf{u}_i$ denoted the velocity. $\mathbf{F}$ is the interaction force between the two phases ($\mathbf{F}_s = -\mathbf{F}_f$). We did not enter the interaction between the air phase and other two phases in this study. The mass conservation Equation (1) implies the following for the slide phase:

$$\rho_s \frac{dV_s}{dt} - \rho_s B s_0(l_s, t) u_0(l_s, t) = 0 \tag{3}$$

For the water phase, the following is defined:

$$\rho_f \frac{dV_f}{dt} + \rho_f \bar{u}_{f,r}(h_0 + \eta_r)B = 0 \tag{4}$$

where ρ_s and ρ_f denote the slide density and water density, respectively; V_s and V_f represent the volume of the slide and water in the control volume, respectively; s_0 and u_0 denote the thickness and velocity of the slide entering the shoreline (left boundary of the control volume), respectively; t is time, B is the flume width, l_s is the slope length, h_0 is the still water depth, and η_r and η_l are the water surface perturbation at the right boundary and left boundary, respectively; $\bar{u}_{f,r}$ denotes the depth average velocity of the water at the right boundary.

The momentum conservation Equation (2) for the slide phase in x direction can be expressed as follows:

$$\rho_s \frac{dV_s \bar{u}_s}{dt} - \rho_s B s u_0^2 \cos\theta = -F_{D,x} + F_{P,x} \tag{5}$$

and in the y direction can be written as follows:

$$\rho_s \frac{dV_s \bar{v}_s}{dt} - \rho_s B s u_0(l_s, t)^2 \sin^2\theta / \cos\theta = -F_{D,y} + F_{P,y} - \rho_s V_s g \tag{6}$$

For the water phase, the momentum conservation in the x direction is as follows:

$$\rho_f \frac{dV_f \bar{u}_f}{dt} + \rho_f \bar{u}_{f,r}^2 (h + \eta_r)B = F_{D,x} - \frac{1}{2}\rho_f g B \left[(h + \eta_r)^2 - (h + \eta_l)^2 \right] \tag{7}$$

and in the y direction is as follows:

$$\rho_f \frac{dV_f \bar{v}_f}{dt} = F_{D,y} \tag{8}$$

On the left hand side of Equation (5), the first term reflects the change rate of the slide's momentum in the control volume, and the second term represents the momentum flux across the left boundary of the control volume. The right-hand sides of Equations (5)–(8) reveal that two mechanisms are at play in the momentum change and transfer to the fluid phase: the momentum imparted by the slide phase through the drag force and the pressure the force difference. For the momentum balance equation of the slide phase in the y direction (Equation (6)), the hydrostatic force was assumed to be balanced with the gravity force, as the density of the slide material used in the experimtheents was close to that of water. For the momentum balance of the water phase in x direction (Equation (7)), the hydrostatic force applied to the water by the submerged slide was considered to be balanced with the hydrostatic force at the right boundary.

The hydrostatic force $\mathbf{F}_P$ can be written in an integral form:

$$\mathbf{F}_P = \int_{A_s} -\rho_f g h_{sf} \mathbf{n} \, dA_s \tag{9}$$

where A_s denotes the area of the slide–water interface, h_{sf} is the vertical distance between the slide–water interface and the free water surface, and $\mathbf{n}$ denotes the normal vector. We approximate the drag force $\mathbf{F}_D$ by the following:

$$\mathbf{F}_D = \frac{1}{2} C_d \rho_f A_f \left(\bar{\mathbf{u}}_s - \bar{\mathbf{u}}_f \right) \mid \bar{\mathbf{u}}_s - \bar{\mathbf{u}}_f \mid \tag{10}$$

where A_f is the effective cross-sectional area of the slide–water interface, C_d is the drag coefficient (we take $C_d = 0.5$), and $\bar{\mathbf{u}}_s$ and $\bar{\mathbf{u}}_f$ are idealized by the mean velocity of the slide phase and water phase in the control volume, respectively. Here, A_f, $\bar{\mathbf{u}}_s$, and $\bar{\mathbf{u}}_f$ are unknown and given by experimental data.

Equations (3)–(8) form a system of six coupled equations that describe the interplay between the slide phase and water phases. The dependence variables include $\bar{u}_s$, $\bar{v}_s$, $\bar{u}_f$, $\bar{v}_f$, V_s, and V_f. Here, we focused on how the momentum was transferred during the interaction. As experiments have shown, the wave generation mainly relies on the momentum transfer in the horizontal direction; Equations (5) and (7) (momentum balance equations for the two phases in the x direction in the defined control volume) are relatively interesting with regard to the overall dynamics. Therefore, Equations (5) and (7) are solved to determine the time variation of the momentum of the two phases in a control volume. The closure equations and boundary conditions of the proposed model will be presented in Section 2.3. The interacting forces, including drag force and hydrostatic force, will be discussed on the basis of the experimental data in Section 4.1. The equations were solved using a finite difference method and programmed using MATLAB 2021.

2.3. Boundary Conditions

For the left boundary of the control volume, the time variation of the slide thickness $s_0(t)$ and the depth average velocity $\bar{u}_0(t)$ entering the control volume should be given. For the right boundary, the outgoing velocity of the fluid $\bar{u}_{f,r}$ and the free surface perturbation η_r must be calculated. Here, we assume that the flow depth averaged velocity is related to the free surface perturbation $\bar{u}_f = C \frac{\eta}{h_0 + \eta}$, with $C = \sqrt{g(h_0 + \eta)}$. We assume that the outgoing velocity is close to the volume-averaged velocity ($\bar{u}_{f,r} = \bar{u}_f$). The closure equation is then

$$\bar{u}_{f,r} = \eta \sqrt{\frac{g}{h_0 + \eta}} \tag{11}$$

and, thus, the free water surface perturbation is

$$\eta_r = \frac{1}{2g} \left(\bar{u}_{f,r}^2 + u_f \sqrt{\bar{u}_f^2 + 4gh_0} \right) \tag{12}$$

The left boundary of the control volume $s_0(t)$ and $\bar{u}_0(t)$ can be given based on the lubrication theory. We consider that the rheological behavior of the sliding mass follows the Herschel–Bulkley law. For a simple shear flow, this law implies that there is motion only when the shear stress τ exceeds a threshold called the yield stress τ_c:

$$\mu \dot{\gamma}^n = \begin{cases} \tau - \tau_c & \tau > \tau_c \\ 0 & \tau \leq \tau_c \end{cases} \tag{13}$$

where $\dot{\gamma}$ is the shear rate, μ is the consistency, and n is a power law index that reflects shear thinning (or shear thickening for the materials n > 1).

For a steady uniform flow of viscoplastic fluid over an inclined surface, independent of the constitutive equation, the shear stress distribution throughout the depth is $\tau(\hat{y}) = \rho g (s - \hat{y}) \sin \theta$, where s denotes the flow depth, and g is the gravitational acceleration. The no-slip condition is assumed for the streamwise velocity component u at

the bottom (i.e., $u(0) = 0$). The integration of the constitutive equation provides the cross-stream velocity profile:

$$u(\hat{y}) = \frac{nA}{n+1} \begin{cases} \left(Y_0^{1+1/n} - (Y_0 - \hat{y})^{1-1/n}\right) & \hat{y} < Y_0 \\ Y_0^{1+1/n} & \hat{y} \geq Y_0 \end{cases} \tag{14}$$

where $Y_0 = s - s_c$, $A = \left(\frac{\rho g \sin\theta}{\mu}\right)^{1/n}$, and $s_c = \tau_c/(\rho g \sin\theta)$. A further integration leads to the depth average velocity:

$$\bar{u} = \frac{nA}{(n+1)(2n+1)} \frac{s(n+1) + ns_c}{s} Y_0^{1+1/n} \tag{15}$$

For the slight nonuniform consideration, with the assumption of negligible inertia, the downstream projection of the momentum balance equation reads as follows: $0 = \rho g \sin\theta - \frac{\partial p}{\partial \hat{x}} + \frac{\partial \tau}{\partial \hat{y}}$; the pressure is found to be hydrostatic to the following leading order: $p = \rho g(s - \hat{y})\cos\theta$. The streamwise velocity component is given by the momentum balance equation:

$$\frac{\partial \tau}{\partial \hat{y}} + \rho g \sin\theta = \rho g \cos\theta \frac{s}{\hat{x}} \tag{16}$$

By substituting τ from the constitutive Equation (13) into Equation (16) and integrating it, the velocity profile can be given:

$$u(\hat{y}) = \frac{nK}{n+1} \left(\tan\theta - \frac{s}{\hat{x}}\right)^{1/n} \begin{cases} \left(Y_0^{1+1/n} - (Y_0 - \hat{y})^{1+1/n}\right) & \hat{y} < Y_0 \\ Y_0^{1+1/n} & \hat{y} \geq Y_0 \end{cases} \tag{17}$$

with $K = \rho a \sin\theta/k$, and $Y_0 = max(0, s - \tau_c/(\rho g \cos\theta(\tan\theta - \partial_x s)))$, which denotes the yield surface. A further integration leads to the depth average velocity:

$$\bar{u} = \frac{nK}{(n+1)(2n+1)} \left(\tan\theta - \frac{\partial s}{\partial \hat{x}}\right)^{1/n} \frac{s(n+1) + ns_c}{s} Y_0^{1+1/n} \tag{18}$$

To capture the time evolution of the frontal position and flow depth, three models of increasing complexity were commonly studied: the kinematic wave model, advection diffusion model, and one-layer Saint-Venant equations. The results indicated that the simplest kinematic wave model had the best agreement with the experimental data [28]. Therefore, here, the kinematic wave model was selected to evaluate the time variation of the slide thickness at the left boundary of the control volume.

Within the frame of the kinematic wave approximation, the flow is assumed to be locally uniform. The variations in the depth-averaged velocity are then dictated by the flow depth alone, $\bar{u} = \bar{u}(s)$, which is given by Equation (15). The bulk mass balance $\frac{\partial s}{\partial \hat{t}} + \frac{\partial s\bar{u}}{\partial \hat{x}} = 0$ provides the governing equation for s:

$$\frac{\partial s}{\partial \hat{t}} + f'(s)\frac{\partial s}{\partial \hat{x}} = 0 \tag{19}$$

with $f'(s) = As(s - s_c)^{1/n}$, and $A = \left(\frac{\rho g \sin\theta}{\mu}\right)^{1/n}$. The hyperbolic nonlinear advection equation can be solved easily using the method of characteristics. Equation (19) can be put into a so-called characteristic form $\frac{ds}{d\hat{t}} = 0$ along the characteristic curve $\frac{d\hat{x}}{d\hat{t}} = f'(s)$. These initial characteristic curves are straight lines whose slopes are dictated by the initial depth:

$$\hat{x} = f'(s_0(\hat{x}_0))\hat{t} + \hat{x}_0 \tag{20}$$

where $s_0(\hat{x}_0)$ is the initial value of s at $\hat{x}_0$. We considered the following initial condition, a volume V_I (per unit width) of the fluid, to be contained in a reservoir of length l_0. The flume inclination is θ. The fluid is at rest with the following initial depth profile:

$$s(\hat{x}, 0) = s_0(\hat{x}) = s_g + (\hat{x} - l_0)\tan\theta \tag{21}$$

with s_g being the depth at the lock gate, while $s_g = V_I/l_0 + \frac{1}{2}l_0\tan\theta$. $s_0(\hat{x}_0)$ is given by Equation (21). As $s = s_0$ along the characteristic curve, and by eliminating $\hat{x}_0$ using Equation (21), an implicit equation for s can be obtained:

$$\hat{x} = As(s - s_c)^{1/n}\hat{t} + (s - s_g)\cot\theta + l_0 \tag{22}$$

As illustrated in Figure 1, the time adjustment between the (x, y) coordinate and $(\hat{x}, \hat{y})$ coordinate is $t = \hat{t} - t_0$, where t exhibits the time since the slide enters the left boundary, and t_0 denotes the time taken from the initial position to the shoreline. t_0 can be obtained from Equation (21).

3. Experimental Method

3.1. Experimental Facilities

As shown in Figure 2, experiments were conducted in a two-part narrow flume. The first part was a chute, 1.5 m long and 0.12 m wide, which could be tilted at angle θ ranging from 30° to 50°. The slide walls of the slope were made of PVC. The second part was a water-filled, transparent, glass flume, 2.5 m long, 0.4 m deep, and 0.12 m wide. The slide material was initially contained in a box located at the chute entrance and closed by a locked gate. This gate could be opened in less than 0.1 s owing to two pneumatically driven pistons. The distance from the gate to the shoreline ranged from 0.5 m to 1.0 m. Once released, the slide material accelerated energetically under gravity and reached velocities as high as 2.5 m/s. In addition, PIV system was built to record the slide–water interaction and the wave generation, which consisted of a laser, four lenses, and two high-speed cameras. As shown in Figure 2a, two high-speed cameras were placed in front of the shoreline with their optical axes perpendicular to the side wall. A black and white camera with a frequency of 400 fps and a resolution of 1280 × 1024 pixels was used to record the motion of water. A color camera with the same frequency and a resolution of 600 × 800 pixels was used to record the motion of sliding mass. As shown in Figure 2b,c, the laser beam first passed a circular lens (I) with a focus length of d = 90 mm; then, it passed a laser line generator lens (II) with a divergence angle of 30° and became a laser sheet; afterwards, the laser sheet passed through a rectangular lens (III) with a focus length of d = 200 mm in the vertical direction and an oblong lens (IV) with a focus length of d = 1.5 m in the horizontal direction. The flume illuminated by the laser sheet is shown in Figure 2e.

Figure 3 displays the principle of the PIV system. The particle-seeded flow was illuminated in a target area with a light sheet, and the velocity vectors were derived from subsections of the target area by measuring the movement of seeding particles between two image frames.

3.2. Slide Material

As for the slide material, a viscoplastic material called Carbopol was used. See Figure 4a,b for the photos of the transparent and colored Carbopol, respectively. Its rheological behavior depends on its concentration and can be described using the Herschel–Bulkley model (see Equation (13)). Here, we used Carbopol with a concentration of 2.5%, with the rheological parameters being τ_c = 74 Pa, μ = 29.1 Pa·s^n, and n = 0.364. See details of the material properties in our previous studies [30,34]. The water body was seeded by polyamide-seeding particles with a diameter of 50 µm, and Carbopol was seeded by fluorescent-seeding particles with a diameter of 20 µm. See [35] for details of the fluorescent-seeding particles technique. Figure 4c,d display the photos of seeded Carbopol and water recorded by PIV system.
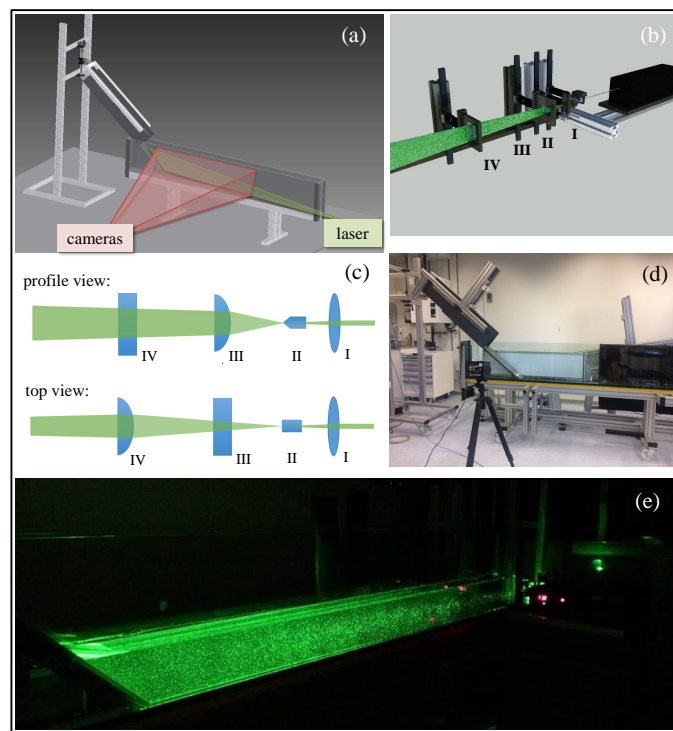
Figure 2. (**a**) Design of the experimental system, (**b**) position of the lens and laser, (**c**) optical design, (**d**) photo of the experimental set up, and (**e**) the flume illuminated by laser sheet.
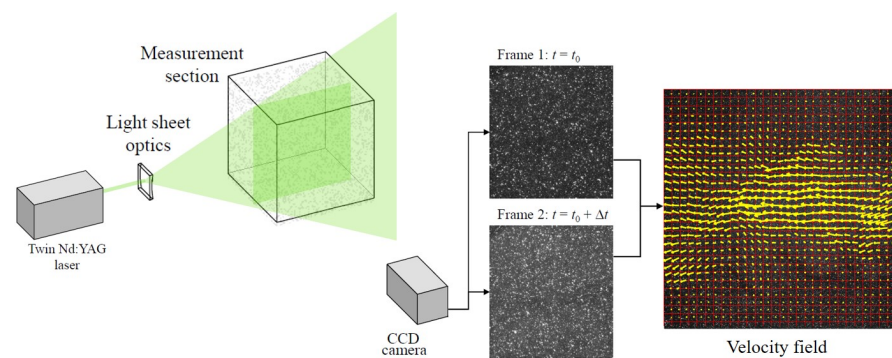
Figure 3. The principle of the PIV system.
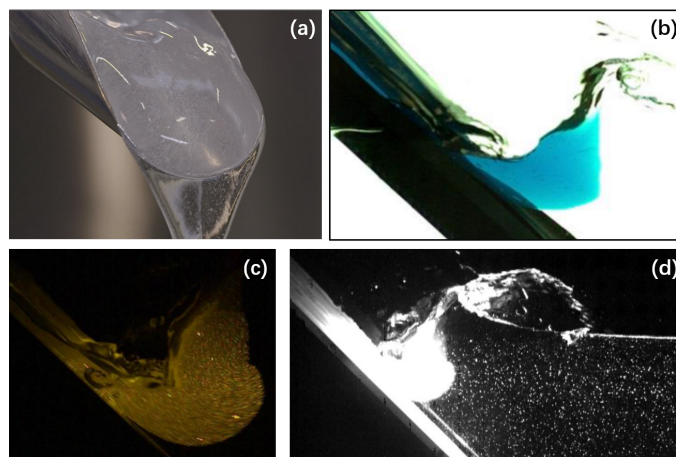
Figure 4. Photos of the (**a**) transparent Carbopol, (**b**) colored Carbopol, (**c**) seeded Carbpol recorded by PIV, and (**d**) seeded water recorded by PIV system.

3.3. Image Processing

The initial settings of each experiment included the slide volume V_i, initial slide length l_0, initial slide height s_0, slope length l_s, still water depth h_0 and slope angle θ , which were been recorded before the slide material was released. We mainly determined two sources information from the PIV experiments: the interface between the slide and water phase and the velocity fields of the two phases. We first detected the areas with seeding particles from the raw images and eliminated the pixels outside of the recognized area. Then, the time variation of the slide–water surface and the free water surface could be obtained. Figure 5 illustrates the evolution of free water surface and slide water interface of an example test whose initial settings were l_s = 0.85 m, $\alpha = \pi/4$, m_I = 4.0 kg, and h_0 = 0.2 m.
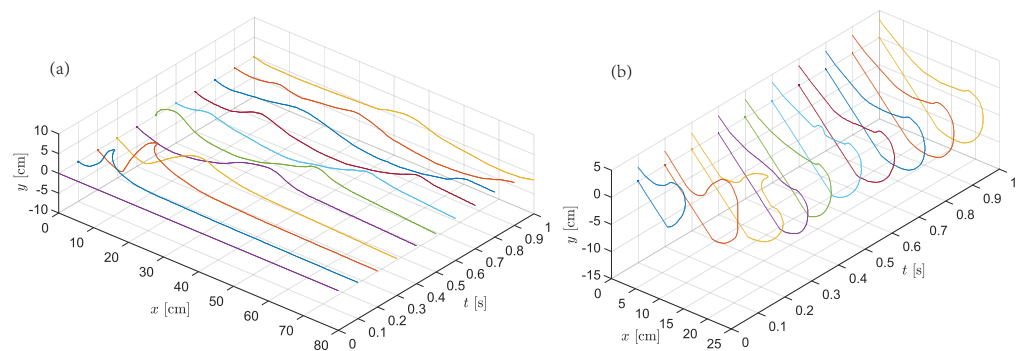
Figure 5. Evolution of (**a**) free water surface and (**b**) slide water interface from t = 0.1 s to 1.0 s.

The velocity field was determined using a toolbox in MATLAB 2021 named *MatPIV*. We used a 32 × 32 pixel interrogation window and a 50% overlap between adjacent windows. To remove the spurious velocity vectors, a range validation filter was used, and all the velocity vectors larger than 3 m/s were discarded. Using a moving average validation filter, the velocity vectors that deviated by 15% from the average value of their surroundings 3 × 3 vectors fields were substituted by interpolation. The velocity vectors were converted into the velocities by calibrating the physical size of a pixel in an image. See details of the processing procedure in our previous work [36]. Figures 6 and 7 display the velocity fields of the submerged Carbopol and water body at the first 0.6 s for the example test. We selected one representative image for each Δt = 0.1 s.

The velocity fields, we estimated the average velocity and momentum of the two phases in a selected area. The average velocity of the material (i.e., slide or water) in a selected area can be calculated by the average velocity of the interrogation windows in the area. The momentum can be calculated by integrating the velocity at each interrogation window. The mean velocity of the material in a selected area can be calculated by the following:

$$(\bar{u}, \bar{v}) = \frac{1}{r} \sum_{i=1}^{r} (\Delta u_i, \Delta v_i) \tag{23}$$

where $\bar{u}$ and $\bar{v}$ refer to the mean velocity of the material in a selected area in the horizontal and vertical direction, respectively, Δu_i and Δv_i are the velocity of the ith interrogation window, i counts the number of interrogation windows, and r refers to the number of interrogation windows contained in the selected area. The material mass in a selected area can be expressed as follows:

$$m_S = \int_S \rho b \, dS = \rho b \sum_{i=1}^{r} \Delta S \tag{24}$$

where S is the area of the selected area, ΔS is the area of an interrogation window, b is the slope width, and ρ refers to the density of the material. The momentum of the material in a selected area can be written as follows:

$$\mathrm{P} = (P_x, P_y) = \int_S m_S \bar{u}_S dS = m_S \sum_{i=1}^{r} (\Delta u_i, \Delta v_i) \tag{25}$$

where P is the momentum of the material, and P_x and P_y denote the momentum in the horizontal and vertical direction, respectively.
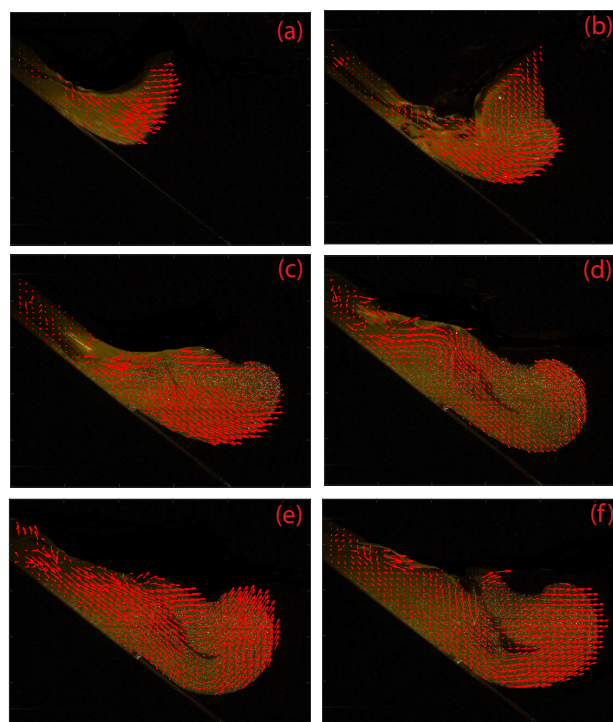
Figure 6. Time variation of velocity field of the submerged landslide: (**a**) t = 0.1 s, (**b**) t = 0.2 s, (**c**) t = 0.3 s, (**d**) t = 0.4 s, (**e**) t = 0.5 s, and (**f**) t = 0.6 s.
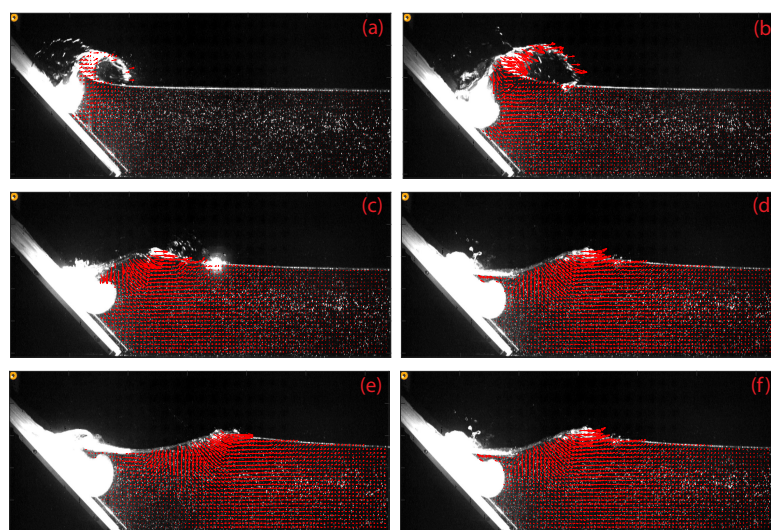
Figure 7. Time variation of velocity field of the water body in the control volume: (**a**) t = 0.1 s, (**b**) t = 0.2 s, (**c**) t = 0.3 s, (**d**) t = 0.4 s, (**e**) t = 0.5 s, and (**f**) t = 0.6 s.

4. Momentum Transfer between the Sliding Mass and the Water Body

This section displays how the momentum is transferred from the slide phase to the water phase by analyzing the interaction forces engaged in stopping the motion of the slide phase and the momentum variations of the two phases in the observation window.

4.1. Interaction Forces

As analyzed in Section 2, the forces governing the momentum transfer mechanism between the sliding phase and water phase consist of two parts: one is the hydrostatic force $\mathbf{F}_P$, the other is the drag force $\mathbf{F}_D$.

4.1.1. Hydrostatic Force

The hydrostatic force $\mathbf{F}_P$ can be experimentally determined from the records of the slide–water interface and free water surface (Figure 5). Due to the complexity of the slide–water interface's evolution, it is difficult to presume a theoretical expression for $\mathbf{F}_P$ directly. The strategy was to determine the force experimentally and then make a mathematical approximation based on the experimental data. An observation window with a length of 0.6 m was selected, which corresponds to the control volume V in the theoretical model. Four representative experiments were selected as examples to display the general tendencies of the results. Table 1 shows the initial parameters of the four selected experiments.

Table 1. Initial parameters of the selected tests, which served as examples.

Test Number	l_s [m]	α [-]	m_I [kg]	h_0 [m]
Test 32	1.05	$\pi/4$	3.0	0.2
Test 40	0.95	$\pi/4$	3.5	0.2
Test 42	0.85	$\pi/4$	4.0	0.2
Test 46	0.85	$\pi/4$	4.5	0.2

Figure 8 shows the time variation of the hydrostatic force $\mathbf{F}_P$ acting on the submerged slide material for the four selected experiments. The horizontal projection of the hydrostatic force $\mathbf{F}_P$ is denoted by $F_{p,x}$, and the vertical projection of $\mathbf{F}_P$ is denoted by $F_{p,y}$. At the very beginning, both $F_{p,x}$ and $F_{p,y}$ increased quickly. Then, $F_{p,x}$ and $F_{p,y}$ began to decrease, with the submerged slide starting to stop and the leading wave starting to decay. After the slide had stopped, $F_{p,x}$ and $F_{p,y}$ were finally balanced with the gravity and the anchorage force provided by the slope.
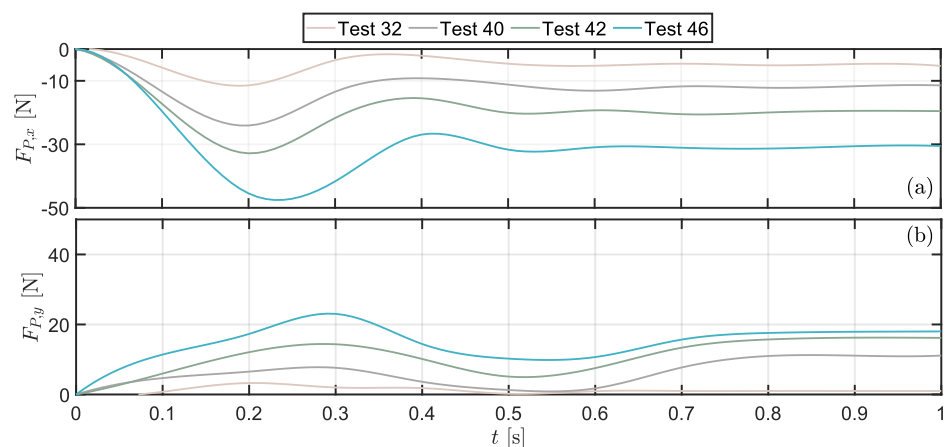
Figure 8. Time variation of the hydrostatic force $\mathbf{F}_P$ acting on the slide phase: (**a**) horizontal projection $F_{p,x}$ and (**b**) vertical projection $F_{p,y}$.

As mentioned in Section 2, the transfer of momentum in the horizontal direction plays a key role in wave formation, so we emphasized the horizontal projection of the hydrostatic

force $F_{p,x}$. As shown in Figure 8, $F_{p,x}$ approximately followed a parabola function that increased quickly at the beginning and began to decrease after reaching the maximum value. The axis of symmetry of the parabola curve in Figure 8 was defined as the acting time t_a, which can be approximated by the time taken from the front of the slide touching the shoreline to the wave reaching its maximum height. Thus, $F_{p,x}$ can be expressed as follows:

$$F_{p,x} = \begin{cases} \frac{4F_{pmx}}{t_a^2}t(t_a - t) & 0 < t < t_a \\ 0 & x > t_a \end{cases} \tag{26}$$

where F_{pmx} is the maximum value of $F_{p,x}$. In this simplified equation, F_{pmx} and t_a were unknown. We then developed empirical equations for F_{pmx} and t_a by regressing the experimental data:

$$F_{pmx} = -25.412s_0^{0.480}u_0^{1.089}m_E^{0.387} \tag{27}$$

$$t_a = 0.358s_0^{-0.051}u_0^{0.243}m_E^{0.003} \tag{28}$$

Here, the slide thickness s_0 and the slide velocity u_0 at impact, as well as the effective mass m_E, have been routinely used to estimate the wave characteristics. Figure 9 displays the measured and predicted maximum hydrostatic force in the x direction of F_{pmx} and acting time t_a. The coefficient of determination R^2 was 0.884 for F_{pmx} and 0.875 for t_a, which means the F_{pmx} and t_a fit well with Equations (27) and (28).
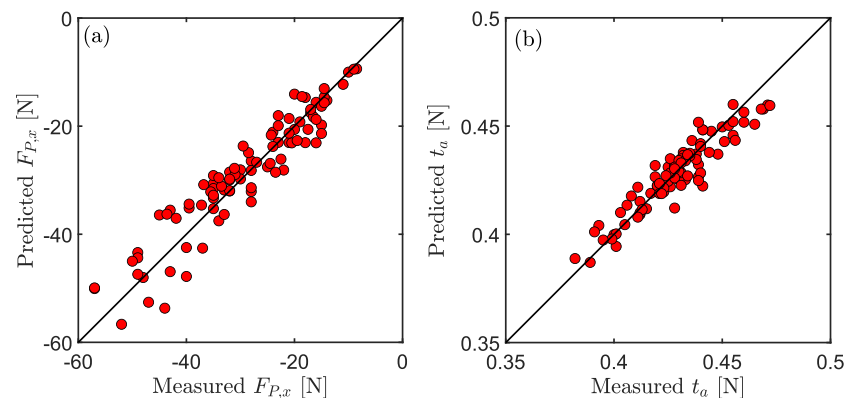
Figure 9. The comparison of the measured and predicted (**a**) F_{pmx} and (**b**) t_a.

4.1.2. Drag Force

The drag force $\mathbf{F}_D$ mainly depends on the velocity difference between the slide material and the body of water. It is also influenced by many other factors, including the shape of the slide–water interface, the slide material's deformability, etc. Equation (10) displays the expression of $\mathbf{F}_D$. In the equation, the effective area of the slide–water interface A_f, the velocity of the submerged slide material $\bar{\mathbf{u}}_s$, and the water velocity $\bar{\mathbf{u}}_f$ are lacking.

As shown in Figure 10a,b, both the horizontal and vertical projections of the center of mass of the submerged slide material decreased from $t = 0.2$ s, thus showing the deformation of the submerged slide material. As the slide is deformable, the velocity at the frontal area is different from the mean velocity of the slide. As a simplification, we estimated the velocity of the two phases by their mean velocity in the control volume. Figure 10e,f show the x and y projection of the mean velocity of the submerged slide, respectively.
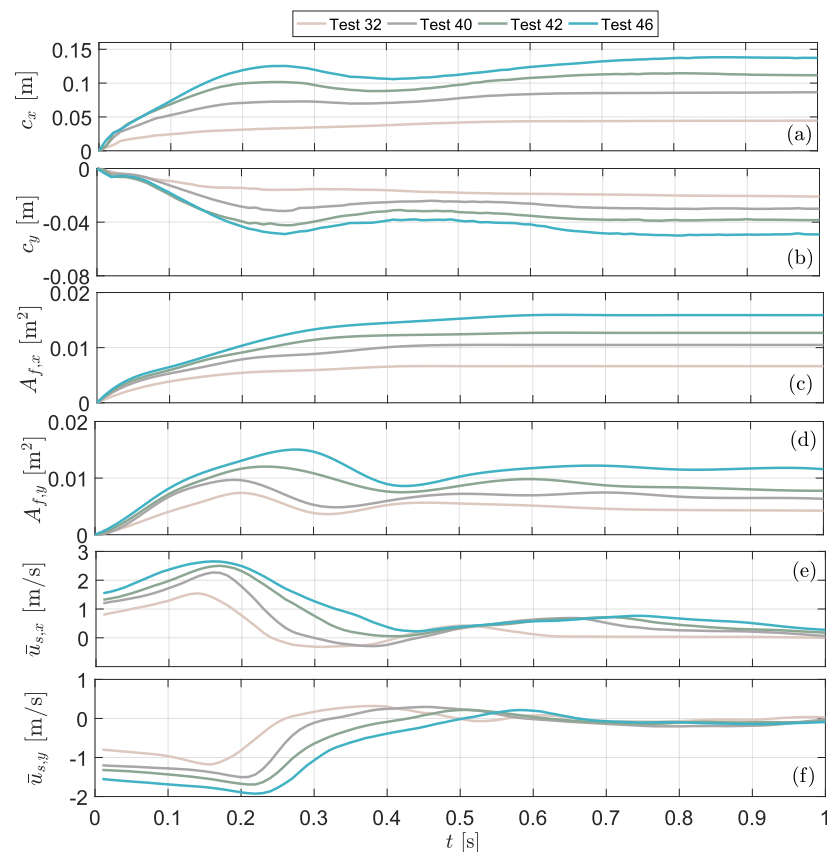
Figure 10. Time variation of the horizontal and vertical projections of the slide's center of mass (**a**) c_x and (**b**) c_y, the frontal area (**c**) A_x and (**d**) A_y, and the mean velocities of submerged mass (**e**) $\bar{u}_x$ and (**f**) $\bar{u}_x$.

Figure 10c,d show the time variatiosn of the horizontal and vertical projections of the frontal area $A_{f,x}$ and $A_{f,y}$. We assume that the x projection of the effective frontal area $A_{f,x}$ followed a parable function. Thus, $A_{f,x}$ can be approximated by the following:

$$A_{f,x} = \begin{cases} \frac{A_{fxm}}{t_a^2}(t - t_a)^2 + A_{fxm} & 0 < t < t_a \\ A_{fxm} & x > t_a \end{cases} \tag{29}$$

where A_{fxm} denotes the maximum value of $A_{f,x}$. The empirical equation of $A_{f,x}$ was obtained by regression with experimental data using s_0, u_0, and m_E:

$$A_{fxm} = 0.038 s_0^{0.985} u_0^{0.067} m_E^{0.098} \tag{30}$$

Figure 11 compares the A_{fxm} measured from the experiments and estimated with Equation (30). The coefficient of determination was $R^2 = 0.891$.

The velocity of the submerged slide material $\bar{\mathbf{u}}_s$ and the velocity of the water in the control volume $\bar{\mathbf{u}}_f$ were unknown parameters not only in the drag force equation, but also in the momentum balance equations. The horizontal mean velocity of the submerged slide $\bar{u}_s$ and the water in the control volume $\bar{u}_f$ could be solved along with the momentum conservation equations.
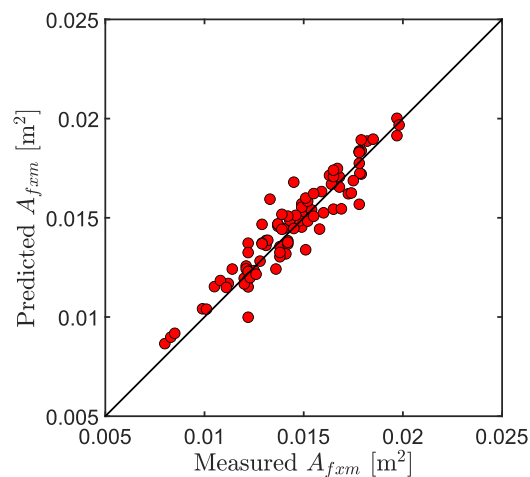
Figure 11. Comparison of the measured and predicted A_{fxm}.

4.2. Momentum Variations of the Sliding Mass and Water Body in the Control Volume

Figure 12 illustrates the momentum variations of the two phases in the observation window for the four selected tests. See Table 1 for the parameters of these four tests. For the momentum of both the slide phase p_s and the water phase p_f, the momentum variations in the horizontal directions $p_{s,x}$ and $p_{f,x}$ were significantly larger than those in the vertical directions $p_{s,y}$ and $p_{f,y}$.
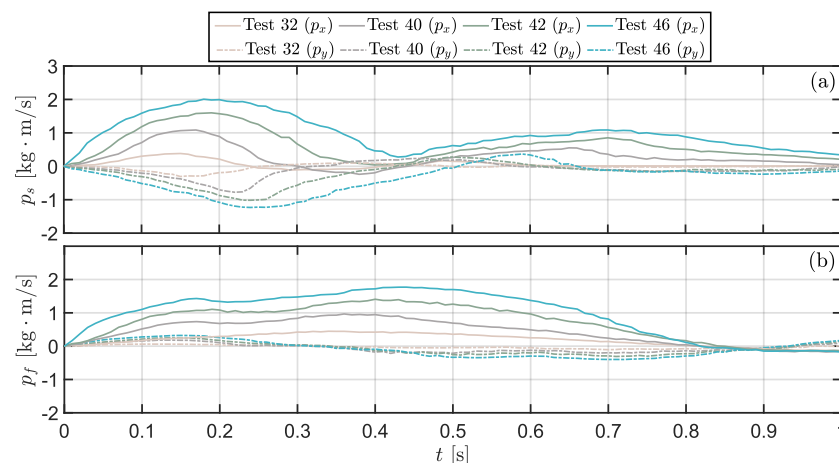
Figure 12. Time variations of the momentum of the (**a**) slide phase p_s and the (**b**) water phase p_f in the observation window.

The theoretical model, which combined the mass and momentum conservation of two-phase flow in a control volume and used viscoplastic theory, has been introduced in Section 2. To validate the expressions of the boundary conditions in the theoretical model, we compared the the s_0 and u_0 obtained from theoretical approximations with the experimental data. Taking Test 42 as an example, Figure 13a,b show the comparison of s_0 and u_0, respectively. The residual between the theoretical data and experimental data was smaller than 10 % for both s_0 and u_0.
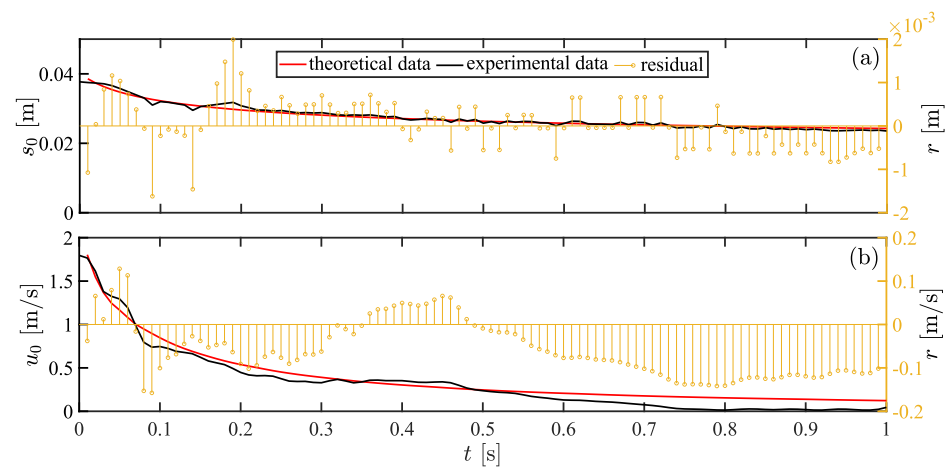
Figure 13. Theoretical and experimental comparison of (**a**) s_0 and (**b**) u_0 with initial parameters varied randomly in the range of 0.85 m $< l_s <$ 1.05 m, 0.15 m $< s_g <$ 0.40 m, 0.2 m $< l_0 <$ 0.4 m, and 60 Pa $< \tau_c <$ 90 Pa.

By knowing the governing equations, boundary conditions (i.e., s_0, u_0, $\bar{u}_{f,r}$, and η_r), and force applied on the control volume (i.e., $F_{D,x}$ and $F_{P,x}$), we can obtain the momentum of the two phases in the control volume by solving Equations (3)–(7). Taking Test 42 as an example, Figure 14a,b compare the experimental slide momentums in the x direction $p_{s,x}$ and the water momentum in the x direction $p_{f,x}$ with their theoretical data. The curves of both $p_{s,x}$ and $p_{f,x}$ fit well with the theoretical results before they reached their maximum values (i.e., $t <$ 0.2 s). The observed $p_{s,x}$ decreased much more sharply than the theoretical curve after $t =$ 0.2 s, and it had a slight rally from 0.4 to 0.6 s. From Figure 14c,d, it can be seen that, with different initial parameters, all the curves followed similar tendencies. $p_{s,x}$ increased during $0 < t <$ 0.2 s and then began decreasing. $p_{f,x}$ increased until $t =$ 0.4 s.
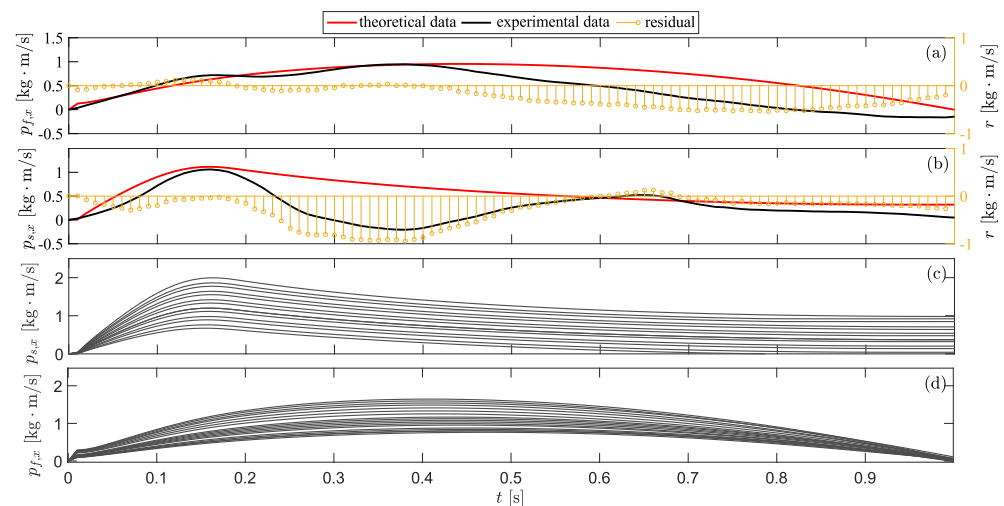
Figure 14. Comparison of (**a**) $p_{s,x}$ and (**b**) $p_{f,x}$ obtained from experiments with the theoretical estimation (Test 42). Theoretical estimations of (**c**) $p_{s,x}$ and (**d**) $p_{f,x}$ with the initial settings 0.85 $< l_s <$ 1.05 m, 0.15 $< s_g <$ 0.40 m, 0.2 $< l_0 <$ 0.4 m, and 60 $< \tau_c <$ 90 Pa.

5. Discussions

5.1. Momentum Transfer and Temporal Wave Characteristics

In addition to the interaction forces and momentum variations, the time series data of the wave amplitude and wave height were measured from experiments. Figures 12 and 15 show that the wave amplitude and height followed similar tendencies with respect to the momentum variations of the submerged sliding mass. Both reached their maximum

values at approximately $t = 0.15$ s. This produces evidence that the time series data of wave characteristics are particularly reliant on the momentum variation of the slide phase. Further, if we look back at Figure 8, it is notable that the increasing stage of $F_{p,x}(t)$ was synchronous with the increasing stage of the wave amplitude $a(t)$. Thus, it would be interesting to provide insights into how the temporal wave characteristics depend on the slide momentum flux passing through the shoreline.
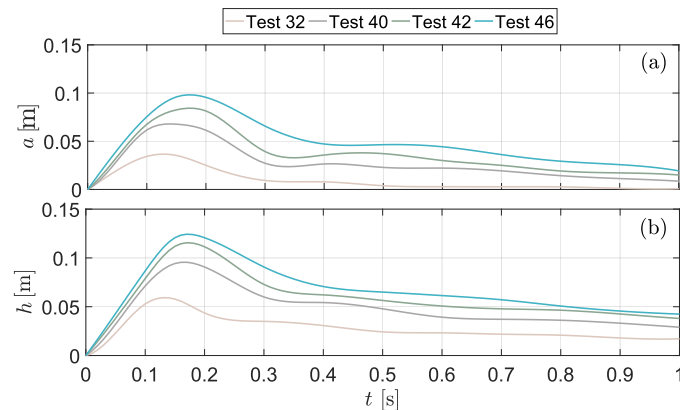
Figure 15. Time variation of (**a**) wave amplitude $a(t)$ and (**b**) wave height $h(t)$.

5.2. Material and Nonmaterial Interfaces

During a landslide entering a body of water, the impulse wave is generated by the momentum imparted by the sliding mass. In this study, we determined the momentum variation of the slide phase and water phase in a control volume. As depicted in Figure 16, two interfaces divided the fluid into three parts: the submerged sliding mass (part I), the moving water body (part II), and the still water body (part III). The material interface between the submerged sliding mass and the water body was a shock wave associated with a density jump. Ahead of this interface, there was a nonmaterial interface, called an acceleration wave, that set the water into motion. Contrary to the frontal shock wave, the velocity and density fields were continuous. Further investigations of the momentum variations according to these two interfaces, instead of assuming a control volume, would be interesting.
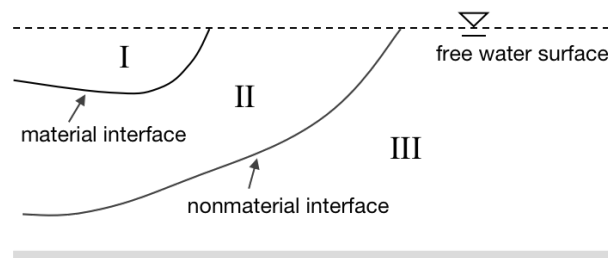
Figure 16. The material and nonmaterial interfaces during the momentum transfer process.

6. Conclusions

The objective of this study was to determine the momentum transfer mechanism during a landslide intruding a body of water. With this objective in mind, we provided an analytical work based on momentum and mass conservation of the phase flow in a control volume. For the unknown parts of the theoretical model, the slide thickness and velocity at the shoreline were estimated based on a viscoplastic theory, and the interaction forces were given by experimental data. Concluding remarks are as follows:

First, the momentum variations in the horizontal direction are significantly larger than those in the vertical direction for both the slide phase and water phase. In addition, the wave generation mainly depends on the momentum transfer from the slide phase to the water

phase in the horizontal direction. The temporal wave amplitude and height are particularly reliant on the momentum variation of the slide phase. In addition, the increasing stage of hydrostatic force is synchronous with the increasing stage of wave amplitude.

Second, the experimental momentum curves of both the slide phase and water phase fit well with the theoretical results before they reached their maximum values (i.e., $t < 0.2$ s). The observed slide momentum in the horizontal direction decreased much more sharply than the theoretical curve after $t = 0.2$ s, and it had a slight rally from 0.4 to 0.6 s. With different initial parameters, all the momentum varying curves in the horizontal direction followed similar tendencies, that is, the slide momentum increased during $0 < t < 0.2$ s and then began decreasing, while the water momentum increased until $t = 0.4$ s.

Third, ahead of the slide–water interface, a nonmaterial interface that sets water into motion was observed from the physical model experiments. That is, we uncovered the interface between the still part and moving part of the water body.

References

1. Kamphuis, J.; Bowering, R. Impulse waves generated by landslides. In Proceedings of the Coastal Engineering, Washington, DC, USA, 13–18 September 1970; pp. 575–588.
2. Heller, V.; Bruggemann, M.; Spinneken, J.; Rogers, B.D. Composite modelling of subaerial landslide–tsunamis in different water body geometries and novel insight into slide and wave kinematics. *Coast. Eng.* **2016**, *109*, 20–41. [CrossRef]
3. Mulligan, R.P.; Take, W.A. On the transfer of momentum from a granular landslide to a water wave. *Coast. Eng.* **2017**, *125*, 16–22. [CrossRef]
4. Le Méhauté, B.; Wang, S. *Water Waves Generated by Underwater Explosion*; World Scientific: Singapore, 1996; Volume 10.
5. Zitti, G.; Ancey, C.; Postacchini, M.; Brocchini, M. Impulse waves generated by snow avalanches: Momentum and energy transfer to a water body. *J. Geophys. Res. Earth Surf.* **2016**, *121*, 2399–2423. [CrossRef]
6. Zhao, L.; Mao, J.; Bai, X.; Liu, X.; Li, T.; Williams, J. Finite element simulation of impulse wave generated by landslides using a three-phase model and the conservative level set method. *Landslides* **2016**, *13*, 85–96. [CrossRef]
7. Yavari-Ramshe, S.; Ataie-Ashtiani, B. A rigorous finite volume model to simulate subaerial and submarine landslide-generated waves. *Landslides* **2017**, *14*, 203–221. [CrossRef]
8. Ruffini, G.; Heller, V.; Briganti, R. Numerical modelling of landslide-tsunami propagation in a wide range of idealised water body geometries. *Coast. Eng.* **2019**, *2019*, 103518. [CrossRef]
9. Fritz, H.M.; Hillaire, J.V.; Molière, E.; Wei, Y.; Mohammed, F. Twin tsunamis triggered by the 12 January 2010 Haiti earthquake. *Pure Appl. Geophys.* **2013**, *170*, 1463–1474. [CrossRef]
10. Grilli, S.T.; Grilli, A.R.; David, E.; Coulet, C. Tsunami hazard assessment along the north shore of Hispaniola from far-and near-field Atlantic sources. *Nat. Hazards* **2016**, *82*, 777–810. [CrossRef]
11. Poupardin, A.; Heinrich, P.; Frère, A.; Imbert, D.; Hébert, H.; Flouzat, M. The 1979 submarine landslide-generated tsunami in Mururoa, French Polynesia. *Pure Appl. Geophys.* **2017**, *174*, 3293–3311. [CrossRef]
12. Fritz, H.M.; Hager, W.H.; Minor, H.E. Landslide generated impulse waves. *Exp. Fluids* **2003**, *35*, 505–519. [CrossRef]
13. Heller, V. Landslide Generated Impulse Waves: Prediction of Near Field Characteristics. Ph.D. Thesis, ETH Zurich, Zurich, Switzerland, 2007.
14. Zitti, G.; Ancey, C.; Postacchini, M.; Brocchini, M. Impulse waves generated by snow avalanches falling into lakes. In Proceedings of the 36th IAHR World Congress, The Hague, The Netherlands, 28 June–3 July 2015; number CONF.
15. Mohammed, F.; Fritz, H.M. Physical modeling of tsunamis generated by three-dimensional deformable granular landslides. *J. Geophys. Res. Ocean.* **2012**, *117*, C11015. [CrossRef]

16. Walder, J.S.; Watts, P.; Sorensen, O.E.; Janssen, K. Tsunamis generated by subaerial mass flows. *J. Geophys. Res. Solid Earth* **2003**, *108*, 2236. [CrossRef]

17. Fernández-Nieto, E.D.; Bouchut, F.; Bresch, D.; Diaz, M.C.; Mangeney, A. A new Savage–Hutter type model for submarine avalanches and generated tsunami. *J. Comput. Phys.* **2008**, *227*, 7720–7754. [CrossRef]

18. Zitti, G.; Ancey, C.; Postacchini, M.; Brocchini, M. Snow avalanches striking water basins: Behaviour of the avalanche's centre of mass and front. *Nat. Hazards* **2017**, *88*, 1297–1323. [CrossRef]

19. Miller, G.S.; Andy Take, W.; Mulligan, R.P.; McDougall, S. Tsunamis generated by long and thin granular landslides in a large flume. *J. Geophys. Res. Ocean.* **2017**, *122*, 653–668. [CrossRef]

20. Franz, M.; Jaboyedoff, M.; Mulligan, R.P.; Podladchikov, Y.; Take, W.A. An efficient two-layer landslide-tsunami numerical model: Effects of momentum transfer validated with physical experiments of waves generated by granular landslides. *Nat. Hazards Earth Syst. Sci.* **2021**, *21*, 1229–1245. [CrossRef]

21. Kim, G.B.; Cheng, W.; Sunny, R.C.; Horrillo, J.J.; McFall, B.C.; Mohammed, F.; Fritz, H.M.; Beget, J.; Kowalik, Z. Three Dimensional Landslide Generated Tsunamis: Numerical and Physical Model Comparisons. *Landslides* **2020**, *17*, 1145–1161. [CrossRef]

22. Fritz, H.M. PIV applied to landslide generated impulse waves. In *Laser Techniques for Fluid Mechanics*; Springer: Berlin/Heidelberg, Germany, 2002; pp. 305–320.

23. Bullard, G.; Mulligan, R.; Carreira, A.; Take, W. Experimental analysis of tsunamis generated by the impact of landslides with high mobility. *Coast. Eng.* **2019**, *152*, 103538. [CrossRef]

24. Zweifel, A.; Hager, W.H.; Minor, H.E. Plane impulse waves in reservoirs. *J. Waterw. Port Coast. Ocean Eng.* **2006**, *132*, 358–368. [CrossRef]

25. McFall, B.C.; Fritz, H.M. Physical modelling of tsunamis generated by three-dimensional deformable granular landslides on planar and conical island slopes. *Proc. R. Soc. A Math. Phys. Eng. Sci.* **2016**, *472*, 20160052. [CrossRef]

26. Evers, F.M.; Hager, W.H.; Boes, R.M. Spatial impulse wave generation and propagation. *J. Waterw. Port Coast. Ocean Eng.* **2019**, *145*, 04019011. [CrossRef]

27. Ancey, C. Plasticity and geophysical flows: A review. *J. Non-Newton. Fluid Mech.* **2007**, *142*, 4–35. [CrossRef]

28. Ancey, C.; Cochard, S. The dam-break problem for Herschel–Bulkley viscoplastic fluids down steep flumes. *J. Non-Newton. Fluid Mech.* **2009**, *158*, 18–35. [CrossRef]

29. Andreini, N.; Epely-Chauvin, G.; Ancey, C. Internal dynamics of Newtonian and viscoplastic fluid avalanches down a sloping bed. *Phys. Fluids* **2012**, *24*, 053101. [CrossRef]

30. Meng, Z. Experimental study on impulse waves generated by a viscoplastic material at laboratory scale. *Landslides* **2018**, *15*, 1173–1182. [CrossRef]

31. Meng, Z.; Ancey, C. The effects of slide cohesion on impulse-wave formation. *Exp. Fluids* **2019**, *60*, 151. [CrossRef]

32. Meng, Z.; Hu, Y.; Ancey, C. Predicting tsunamis generated by gravity-driven mass flows using a data-driven approach. *Water* **2020**, *12*, 600. [CrossRef]

33. Ancey, C.; Andreini, N.; Epely-Chauvin, G. Viscoplastic dambreak waves: Review of simple computational approaches and comparison with experiments. *Adv. Water Resour.* **2012**, *48*, 79–91. [CrossRef]

34. Meng, Z.; Li, X.; Han, S.; Wang, X.; Meng, J.; Li, Z. The Motion and Deformation of Viscoplastic Slide while Entering a Body of Water. *J. Mar. Sci. Eng.* **2022**, *10*, 778. [CrossRef]

35. Müller, A.; Dreyer, M.; Andreini, N.; Avellan, F. Draft tube discharge fluctuation during self-sustained pressure surge: Fluorescent particle image velocimetry in two-phase flow. *Exp. Fluids* **2013**, *54*, 1514. [CrossRef]

36. Meng, Z.; Zhang, J.; Hu, Y.; Ancey, C. Temporal Prediction of Landslide-Generated Waves Using a Theoretical-Statistical Combined Method. *J. Mar. Sci. Eng.* **2023**, *11*, 1151. [CrossRef]